Capacitive Charge-based Self-Sensing for Resonant Electrostatic MEMS mirrors

Richard Schroedter[*] Han Woong Yoo[*] David Brunner[*]
Georg Schitter[*]

[*] *Automation and Control Institute, Technical University of Vienna,
1040 Vienna, Austria
(e-mail: {schroedter, yoo, brunner, schitter}@acin.tuwien.ac.at).*

Abstract: This paper proposes capacitive charge-based self-sensing by integration of the comb drive intrinsic displacement current for resonant electrostatic MEMS mirrors in order to solve the problem of robust feedback for laser scanning in mobile *light detection and ranging* (Lidar) application. A two-channel switched current integrator circuit is implemented to determine the deflection angle and to distinguish the rotation direction from the asymmetric comb drive charge. Parameters of the MEMS mirror are calibrated with the deflection angle by an optical PSD setup. The resonant electrostatic MEMS mirror is parametrically driven by a square wave high voltage signal, which means, that the charge measurement is only available during the time with non-zero drive signal. From the partly available charge measurements, a nonlinear observer is developed to estimate the mirror state at all time for a potential feedback control. The feasibility for online position estimation is proven by simulation using experimental charge and deflection angle measurements resulting in less than 2 % error at full amplitude operation. Finally, the performance of the proposed method is discussed for realization of active MEMS mirror feedback control, overcoming imprecise motions due to structural nonlinearities as well as external disturbances like vibration and climate variation.

Keywords: Resonant MEMS mirror, electrostatic comb drive, capacitive charge sensing, nonlinear observer with switched input

1. INTRODUCTION

MEMS mirrors are broadly applied for high frequent laser scanning applications like video projectors, cf. Urey et al. (2013), 3D distance sensors, cf. Sandner et al. (2010), and external cavity lasers, cf. Ostendorf et al. (2016). Resonant MEMS scanners enable the construction of low-cost and robust mobile automotive *Light Deflection And Ranging* (Lidar) systems, achieving high mechanical deflection angles of 15 °, cf. Yoo et al. (2018). Nevertheless, due to structural nonlinearities in stiffness, damping and capacitance as well as external disturbances like vibration and climate variation, control methods are required for reliable operation, cf. Schroedter et al. (2017). MEMS mirror feedback with additional sensors have several disadvantages. Piezoresistive sensors suffer from relevant temperature dependency and require additional processing steps, cf. Grahmann et al. (2016). Optical feedback result in bulky setups with challenges in precise alignment of the assembly, cf. Baumgart et al. (2015). Piezoelectric sensors, cf. Gu-Stoppel et al. (2017), use not CMOS-compatible manufacturing technology. In contrast, capacitive self-sensing is simple, low-cost and robust for electrostatic MEMS scanners, since it only depends on the electrostatic comb drive geometry, which is extremely precise in semiconductor micro fabrication.

Out-of-plane sensing electrodes investigated in Rombach et al. (2015) provide low sensitivity at the same voltage level compared to in-plane driving combs. Chen et al. (2019) and Brunner et al. (2019) propose self-sensing by current measurements using a transimpedance amplifier with and without sensing combs. However, the displacement current stands in relation to the deflection speed, while its integration provides a deflection angle sensitive charge measurement. Commonly charge sensing approaches like in Yazdi et al. (2004); Chemmanda et al. (2014); Hung et al. (2015) apply a high frequent voltage in MHz-range on top of the drive voltage and demodulate the position with lock-in principle, but they suffer from delays and distortion of the filtered signal. Whereas Roscher et al. (2003) reports self-sensing by direct charge measurement, detecting the half width of the capacitance variation curve.

The contribution of this paper is a novel capacitive charge self-sensing for resonant electrostatic MEMS mirrors using a nonlinear observer. The charge, integrated from the comb drive intrinsic displacement current, determines the mirror position. The electrode charge is calibrated with the deflection angle measured in an optical PSD setup, cf. Yoo et al. (2019). Since resonant MEMS mirrors are driven in parametric resonance with a square wave voltage, the position measurement is only available during none zero voltage phase. Therefore, the charge measurement is fed into a nonlinear observer estimating the mirror state for feedback control. Compared to current sensing reported by Brunner et al. (2019), the proposed method can be

less sensitive to high frequency distortion or noise due to the integration. A two-channel current integrator circuit is implemented to distinguish the rotation direction from the comb drive asymmetries. The feasibility for online position estimation is proven in a simulation using experimental measurement data for charge and deflection angle.

The paper is organized as follows: Section 2 presents the resonant MEMS mirror model and parameter identification. The capacitive charge sensing method and calibration is described in Section 3. Section 4 proposes a switched nonlinear observer for continuous position estimation due to the switching resonant driving principle and shows simulation results using measured charge data. Section 5 gives a discussion on performance and feasibility of the proposed charge sensing. The paper is concluded in Section 6.

2. RESONANT MEMS MIRROR

The 1D resonant MEMS mirror is micro-fabricated from single-crystalline silicon and designed for reliable operation in automotive Lidar, cf. Yoo et al. (2018). The fixed electrostatic comb electrodes have two layers enabling amplitude detection from the displacement current measurement as described by Druml et al. (2018). The mirror is driven with a square wave voltage. A proprietary leaf-spring design, cf. Van Lierop and Khah (2019), introduces progressive stiffening with a highly nonlinear frequency-amplitude behavior. This enables direct zero-crossing detection by the displacement current for operation in the top response curve of the bifurcation, cf. Brunner et al. (2019). In contrast to narrow bandwidth reported by Sandner et al. (2004), the stiffening enables operation in a wide bandwidth at high deflection, which is advantageous for feedback control and synchronization of multiple scanners.

2.1 Modeling

The resonant MEMS mirror is modeled with a single degree of freedom nonlinear oscillation differential equation

$$\ddot{\theta} + \underbrace{\frac{c_n(\theta, \dot{\theta})}{J}}_{\tilde{c}_n(\theta, \dot{\theta})} \dot{\theta} + \underbrace{\frac{k_n(\theta)}{J}}_{\tilde{k}_n(\theta)} \theta = \underbrace{\frac{1}{2J}\frac{\partial C(\theta)}{\partial \theta}}_{\tilde{C}'(\theta)} v^2, \quad (1)$$

where J denotes the torque inertia including the mirror and all moving drive combs, $c_n(\theta, \dot{\theta})$ is a nonlinear damping and $k_n(\theta)$ a high order nonlinear stiffness. All comb capacitances are summarized in $C(\theta)$ showing decreasing value for higher deflection. Due to in-plane configuration, the scanner operates only in parametric resonance. This means a square wave voltage is applied to pull the mirror towards zero deflection and switched off at or shortly after zero crossing to enable a free oscillation, cf. Schenk et al. (2000). The rectangular geometry of the springs as well as the stiffening leaf-springs cause a prominent progressive stiffness. The high nonlinearity in stiffness leads to a bifurcation phenomena in the amplitude-frequency behavior switching between bottom to top response curve sweeping down the frequency, as shown in Fig. 1.

Resonant MEMS mirrors typically show a nonlinear damping due to different damping behavior for immersed and not immersed combs as Klose et al. (2006) describes. In case of the proposed self-sensing method a precise model
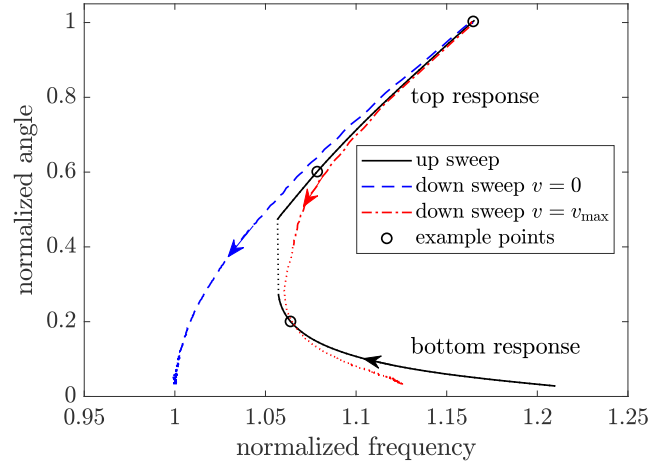

Fig. 1. Nonlinear frequency amplitude behavior. The down sweep $v = v_{\max}$ is corrupted by a drop of drive voltage at small angles $\theta/\theta_{\max} < 0.5$, which is neglected for calibration.

of the actuator capacitance is required and is therefore calibrated using a PSD setup as described in the next section.

2.2 Parameter identification

The nonlinear stiffness and damping curves are evaluated from the free oscillation decay measurement shown in Fig. 2a. The small angle stiffness is calculated from the frequency at the end of the oscillation with $k_0 = J \cdot (2\pi f_0)^2$. The nonlinear stiffness, arising from the leaf-springs, is modeled with four even stiffness coefficients

$$k_n(\theta) = k_0 + k_2\,\theta^2 + k_4\,\theta^4 + k_6\,\theta^6, \quad (2)$$

providing a sufficient representation of the system behavior. The coefficients are identified by matching the potential energy of each period to the backbone curve, cf. down sweep $v = 0$ in Fig. 1, of the free decay using (2) in a nonlinear optimization, as proposed in Brunner et al. (2019). Here, the comparably small damping is neglected. The resulting nonlinear stiffness is shown in Fig. 2b.

An averaged damping coefficient is calculated for each period along the decay, leading to an amplitude dependent
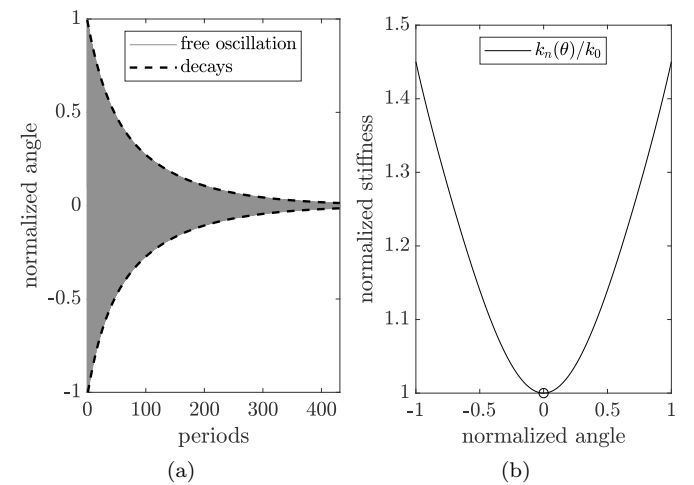

Fig. 2. Decay data and identified stiffness: (a) free oscillation decay with envelope and (b) nonlinear stiffness
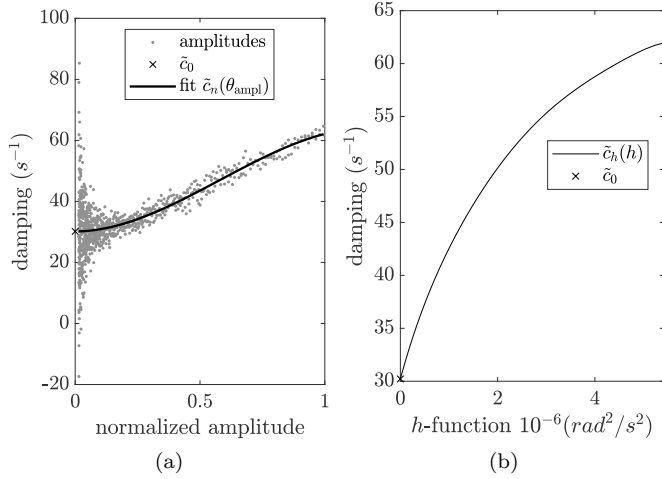
(a)　　　　　　　　　(b)

Fig. 3. Nonlinear damping: (a) amplitude depended damping with polynomial fit $\tilde{c}_n(\theta_{\mathrm{ampl}})$ and (b) h-function depended damping $\tilde{c}_h(h)$

curve shown in Fig. 3a. Because the oscillation amplitude θ_{ampl} of the nonlinear oscillation is not known at every time, the squared velocity $\dot{\theta}$ is low-pass filtered giving a good estimation for the amplitude. For this purpose Brunner et al. (2019) proposes the filter

$$\ddot{h}(t) + 2\,\omega_h\,\dot{h}(t) + \omega_h^2\,h(t) = \omega_h^2\,\dot{\theta}^2(t) \qquad (3)$$

with a bandwidth chosen at about half the oscillation frequency $\omega_h < 4\pi f_0$, which is four times the frequency of $\dot{\theta}^2$. This is a reasonable trade-off between high frequency suppression and fast amplitude estimation. Finally, the fitted damping curve given in Fig. 3a is rewritten in terms of the new h-function as follows

$$\tilde{c}_h(h) = \tilde{c}_0 + \tilde{c}_1\,h + \tilde{c}_2\,h^2 + \ldots + \tilde{c}_6\,h^6, \qquad (4)$$

and is plotted in Fig. 3b.

3. CAPACITIVE CHARGE SENSING

Fig. 4 sketches the realized capacitive charge sensing and observer. The mirror electrode is driven with a square wave voltage v between zero and $v_{\max}$. Between stationary comb electrodes and ground potential, two integrators collect the capacitors displacement current. The voltages v_{A} and v_{B} after integration equal to the charges on comb drives. The upper right and lower left electrodes (red) and vice versa (blue) are connected, to maximize the signal for direction detection. The direction detection is also possible with single-layer combs, that are slightly staggered out-of-plane with respect to the mirror electrode.

The two-channel integrated circuit (ACF2101, Texas Instruments, Texas, US) is applied for current integration. The internal capacitance is enhanced to $C_{\mathrm{int}} = 168\,\mathrm{pF}$ by an external parallel capacitor $68\,\mathrm{pF}$ to fit the voltage amplitude to the analog digital converters (U2542A, Agilent Technologies Inc., Santa Clara, US, $2\,\mathrm{MHz}$ sampling frequency) input. The displacement currents i_{A} and i_{B} are integrated in the capacitance C_{int}, while the operational amplifier creates the voltages v_{A} and v_{B}:

$$v_{\mathrm{A,B}} = -\frac{1}{C_{\mathrm{int}}} \int i_{\mathrm{A,B}}\,\mathrm{d}t. \qquad (5)$$
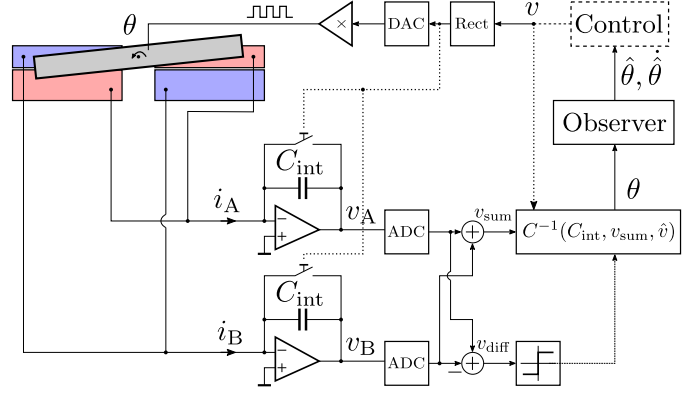

Fig. 4. Charge sensing principle showing the two-layer comb drive connected to two current integrators, and further data processing to observer, control and driver

The sum voltage v_{sum} gives the total charge, while the difference voltage v_{diff} provides the direction of the deflection angle (cf. Fig. 7 (left)):

$$v_{\mathrm{sum}} = v_{\mathrm{A}} + v_{\mathrm{B}}, \qquad v_{\mathrm{diff}} = v_{\mathrm{A}} - v_{\mathrm{B}}. \qquad (6)$$

The deflection angle is calculated using the calibrated inverse capacitance function (cf. Fig. 6) as:

$$\theta = \mathrm{sign}(v_{\mathrm{diff}}) \cdot C^{-1}\left(\left|C_{\mathrm{int}} \cdot \frac{v_{\mathrm{sum}}}{v}\right|\right), \quad \text{for} \quad v \neq 0. \qquad (7)$$

3.1 Sensing calibration

For charge self-sensing the angle dependent transducers capacitance $C(\theta)$ is calibrated once, because the inverse function is used in (7). Therefore, the current integrator outputs and mirror amplitude are measured while the mirror performs an actuated decay (Brunner et al. (2019)) at high deflection angles, where the drive voltage is hold on at $v = v_{\max}$. The measurement data at the start of the decay are demonstrated in Fig. 5 with the decaying angle measured by PSD and the current integrator voltage v_{A}. The second integrator channel voltage v_{B} behaves similar and is omitted for visibility.

While the integrator holds only a small leakage current, the internal MEMS mirror and driving circuit leakages lead to a relevant voltage drop as given in Fig. 5 (bottom). Therefore, an exponential fit is performed for the measurement minimums (blue crosses) and applied to correct the calibration data. The capacitance is given by the following relation:

$$C_{\mathrm{A,B}} = -C_{\mathrm{int}} \cdot \frac{v_{\mathrm{A,B}}}{v_{\max}}. \qquad (8)$$

In Fig. 6 an accurate overlay of at least 20 periods for the evaluated capacitance function can be observed. While the sum capacitance $C = C_{\mathrm{A}} + C_{\mathrm{B}}$ is a measure for the deflection angle, revealing the typical capacitance maximum for resonant in-plane comb drives at zero angle. The sign of $C_{\mathrm{A}} - C_{\mathrm{B}}$ is related to the direction of mirror deflection angle.

3.2 Calibration verification

For verification, the calibrated inverse capacitances are applied to the measurement charge sensing data according to (7) as shown in Fig. 7 for three different amplitudes at $\theta_{\mathrm{ampl}} = [20, 60, 100]\,\%$, marked with circles in Fig. 1.
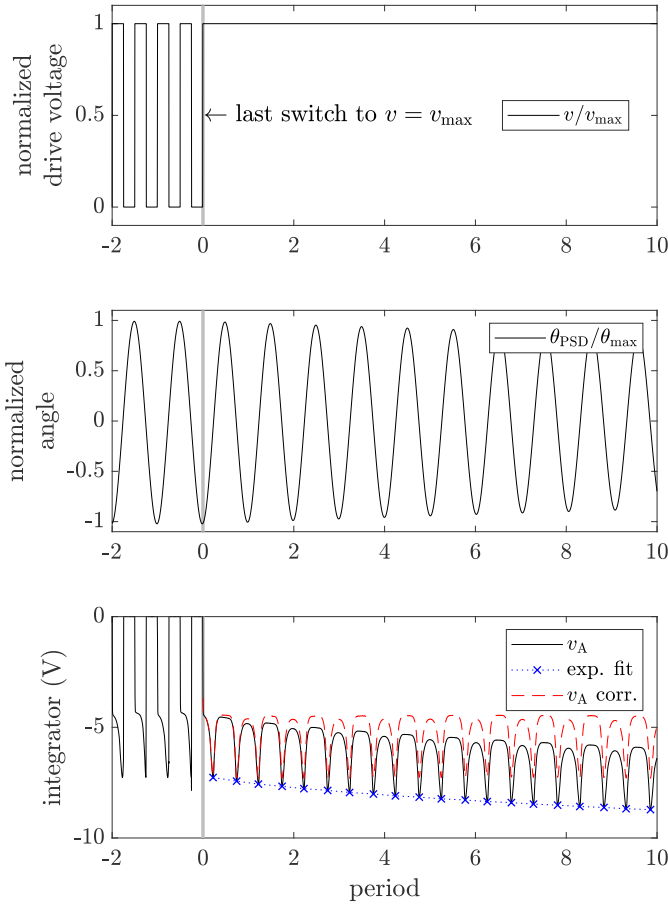
Fig. 5. Measurement result decaying mirror amplitude with PSD (top) and current integrator output (bottom)
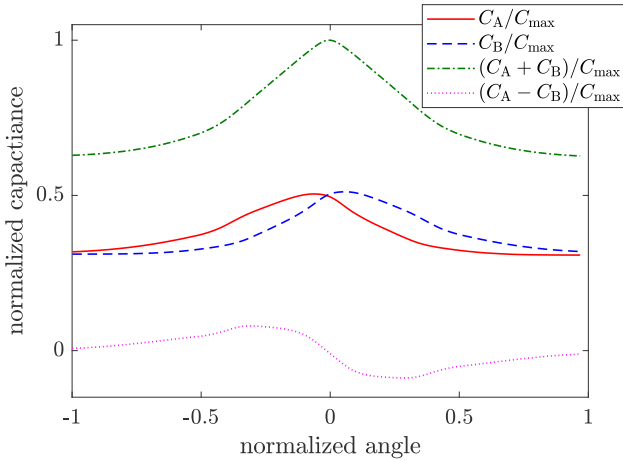
Fig. 6. Capacitance function $C = C_A + C_B$ calibrated with PSD and normalized to $C_{max} = \max\{C_A + C_B\}$

During drive voltage-on times, a high agreement of the charge-sensed deflection with the measured PSD angle can be observed in Fig. 7 (right) after some transient time. Considering a small and constant time delay turned out to be sufficient for suppressing loading transients of the drive and parasitic capacitances. Furthermore, Fig. 7 clarifies, that only half of the period is measured, because the drive voltage needs to be switched off for resonant operation. In the bottom response, cf. Fig. 7 (top), the region around
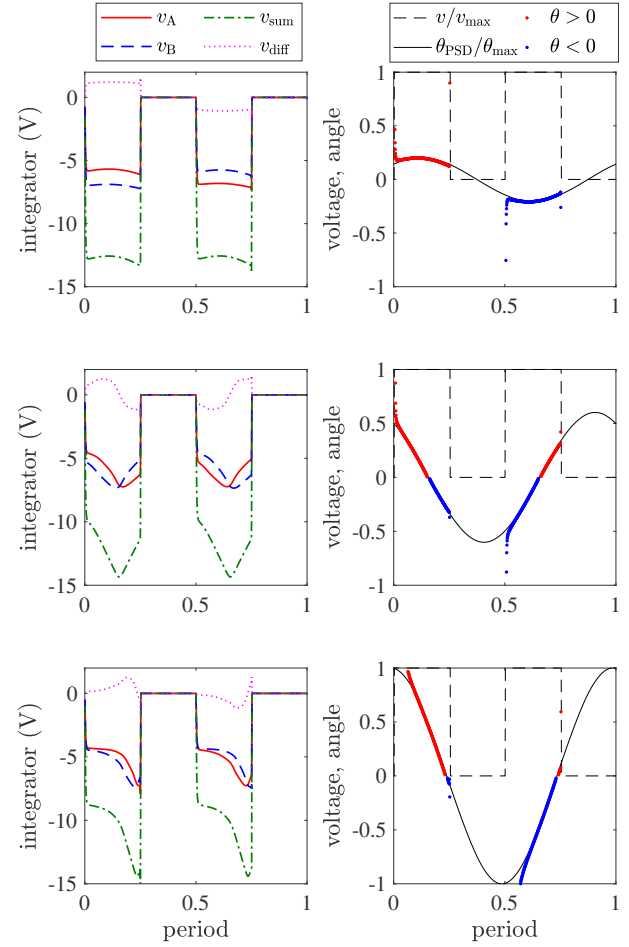
Fig. 7. Calibration applied to measurement data for three different amplitudes θ_{ampl} with integrator voltage (left) and normalized drive voltage and angle (right): 20% (top) , 60% (middle), 100% (bottom)

the oscillation maximum is measured and the voltage is switched off before zero crossing. On the contrary in the top response, cf. Fig. 7 (middle and bottom), the region around zero crossing is measured, but not the oscillation maximum.

4. SWITCHED NONLINEAR OBSERVER

In order to generate a continuous mirror position, a switched nonlinear observer is proposed. The observer gain is only active during the time where the drive voltage is high.

4.1 Observer design

The nonlinear observer is derived using the nonlinear differential equation (1) and the h-function for amplitude estimation using (3). Hence both differential equations are combined in the state $\hat{\boldsymbol{x}}^{\mathrm{T}} = \left[\hat{\theta}, \dot{\hat{\theta}}, h, \dot{h}\right]^{\mathrm{T}}$. The inputs are the drive voltage $u = v$ and the deflection angle y derived from (7). The nonlinear observer equations are as follows:

$$\dot{\hat{\boldsymbol{x}}} = \boldsymbol{A}(\hat{\boldsymbol{x}}) \cdot \hat{\boldsymbol{x}} + \boldsymbol{B}(\hat{\boldsymbol{x}}, u) + \boldsymbol{L} \cdot (\hat{y} - y) \tag{9a}$$

$$\hat{y} = \boldsymbol{c}^{\mathrm{T}} \cdot \hat{\boldsymbol{x}}, \tag{9b}$$

Fig. 8. Nonlinear observer (9), with switch before observer gain to enable and disable correction according to the drive voltage state

with the coefficients

$$A(\hat{x}) = \begin{bmatrix} 0 & 1 & 0 & 0 \\ -\tilde{k}_n(\hat{x}_1) & -\tilde{c}_h(\hat{x}_3) & 0 & 0 \\ 0 & 0 & 0 & 1 \\ 0 & \omega_h^2\,\hat{x}_2 & -\omega_h^2 & -2\,\omega_h \end{bmatrix}, \quad (10a)$$

$$B\left(\hat{x}, u\right) = \begin{bmatrix} 0 \\ \tilde{C}'(\hat{x}_1)\,u^2 \\ 0 \\ 0 \end{bmatrix}, \quad c = \begin{bmatrix} 1 \\ 0 \\ 0 \\ 0 \end{bmatrix}, \quad L^{\mathrm{T}} = \begin{bmatrix} l_1 \\ l_2 \\ 0 \\ 0 \end{bmatrix}. \quad (10b)$$

Note in (10), that the damping $\tilde{c}_h(\hat{x}_3 = h)$ uses the amplitude estimation with the h-function. The designed observer (9), illustrated in Fig. 8, has a typical structure, but with nonlinear matrices $A(\hat{x})$ and $B\left(\hat{x}, u\right)$. Furthermore, a switch is applied before the observer gain L to enable and disable the correction according to the drive voltage state on or off, including a short constant transient time to avoid the transients depicted in Fig. 7. The observer gain is chosen to be $l_1 = \lambda$, $l_2 = \lambda^2$ with $\lambda = 5.5 \cdot 2\,\pi\,f_0$.

4.2 Observer simulation with measurement data

The proposed observer is verified in a Matlab/Simulink simulation ($f_{\mathrm{sample}} = 2\,\mathrm{MHz}$) applying real measured current integrator signals v_A and v_B (including measurement noise), cf. Fig. 7, as input. For reduction of the calculation time, the observer itself is implemented in C using a Matlab mex-function. The observer integrators are initialized with zero. The simulation result for 100 % amplitude shown in Fig. 9 proves a fast convergence to 1.82 % residual error towards the full amplitude within 3 periods. Table 1 summarizes the results, that prove valid operation at top and bottom response curve, cf. Fig. 1.

Table 1. Observer error for three amplitudes: (a) real measured input y from charge sensing and (b) ideal input y from PSD. The error is normalized to deflection amplitude and compared to PSD signal.

	20 % amplitude	60 % amplitude	100 % amplitude
(a) charge sensing err.	7.21 %	2.46 %	1.82 %
(b) PSD angle err.	4.13 %	2.15 %	0.98 %

In Table 1, the observer performance for the input y with the measured charge sensing signal (a) according to (7) is compared to the nominal measured PSD angle (b). The errors in case (b) are mainly caused by the time delay of the observer representing the minimum achievable error.

Fig. 9. Observer simulation result for 100 % amplitude; integrators initialized with zeros: measured integrator outputs (top), measured PSD and charge sensing (Sens.) as well as observer (Obs.) (middle), errors (bottom)

In comparison, the errors from charge sensing in case (a) stay below double of the observation errors from case (b) confirming small noise from the charge measurement data.

5. DISCUSSION

The proposed capacitive charge sensing using a switched integrator requires little implementation effort. The capacitance calibration may be also valid for a whole wafer considering minor etching variation during manufacturing. Since self-sensing is based on the comb capacitance geometry, high robustness towards climate changes is implied. In comparison to current sensing (cf. Chen et al. (2019)), the proposed charge sensing method is less sensitive to high frequent noise and vibrations due to integration. Capacitive charge sensing can operate with and without stiffening or degressive springs, because zero-crossing detection used for current sensing is not required here. To further decrease residual observation errors, cf. Table 1, the leakage current could be reduced or modeled accurately. In summary it was shown, that capacitive charge self-sensing with nonlinear observer provides the mirror state and, thus, is applicable for feedback control of the mirror amplitude and phase for precise laser shooting, e.g. in Lidar application.

6. CONCLUSION

In this paper, the feasibility of a novel capacitive charge-based self-sensing method for position estimation of resonant electrostatic MEMS mirrors is proved. First, the nonlinear stiffness and damping parameter are calibrated from free oscillation decay using optical PSD measurements. The charge is measured by two switched integrators, providing the integral of the comb drive displacement current and the comb drive capacitance. During charge sensing operation a constant transient time is considered to suppress residual loading effects and leakage currents. Second, an appropriate nonlinear observer operates simultaneously for online position estimation, since the measurement signal is only available during half the period time at voltage-on time. The designed observer shows a short transient time of about 3 periods and a small residual error of less than 2% at full angle operation when applying measurement data to an observer simulation. The sensing method is low-sensitive to high frequency noise or vibration compared to current sensing and a good candidate for feedback control. For online MEMS mirror control, both sensing and control can be implemented in a fast processing unit like FPGA realizing Megahertz sampling frequency.

REFERENCES

Baumgart, M., Lenzhofer, M., Kremer, M.P., and Tortschanoff, A. (2015). Integrated packaging of 2D MOEMS mirrors with optical position feedback. In *Proc. of SPIE, MOEMS and Miniaturized Systems XIV*, volume 9375, 93750R.

Brunner, D., Yoo, H.W., Thurner, T., and Schitter, G. (2019). Data based modelling and identification of nonlinear SDOF MOEMS mirror. In *Proc. of SPIE, MOEMS and Miniaturized Systems XVIII*, volume 10931, 1093117.

Chemmanda, L.J., Jianrong, C.C., Singh, R.P., and Roterman, Y. (2014). ASIC front-end for sensing MEMS-mirror position. In *Proc. of Symposium on Integrated Circuits (ISIC)*, 396–399.

Chen, Y., Li, H., Qiu, Z., Wang, T., and Oldham, K.R. (2019). Improved Extended Kalman Filter Estimation using Threshold Signal Detection with a MEMS Electrostatic Microscanner. *IEEE Transactions on Industrial Electronics*, 67(2).

Druml, N., Maksymova, I., Thurner, T., Van Lierop, D., Hennecke, M., and Foroutan, A. (2018). 1D MEMS Micro-Scanning LiDAR. In *Proc. of Conf. on Sensor Device Techn. and Appl. (SENSORDEVICES)*, 48–53.

Grahmann, J., Dreyhaupt, A., Drabe, C., Schroedter, R., Kamenz, J., and Sandner, T. (2016). MEMS-mirror based trajectory resolution and precision enabled by two different piezoresistive sensor technologies. In *Proc. of SPIE, MOEMS and Miniaturized Systems XV*, volume 9760, 976006.

Gu-Stoppel, S., Giese, T., Quenzer, H.J., Hofmann, U., and Benecke, W. (2017). PZT-Actuated and -Sensed Resonant Micromirrors with Large Scan Angles Applying Mechanical Leverage Amplification for Biaxial Scanning. *Micromachines*, 8(215).

Hung, A.C.L., Lai, H.Y.H., Lin, T.W., Fu, S.G., and Lu, M.S.C. (2015). An electrostatically driven 2D micro-scanning mirror with capacitive sensing for projection display. *Sensors and Actuat. A: Physical*, 222, 122–129.

Klose, T., Sandner, T., Schenk, H., and Lakner, H. (2006). Extended damping model for out-of-plane comb driven micromirrors. In *Proc. of SPIE, MOEMS Display, Imaging, and Miniaturized Microsystems IV*, volume 6114, 61140J 61140J.

Ostendorf, R., Butschek, L., Hugger, S., Fuchs, F., Yang, Q., Jarvis, J., Schilling, C., Rattunde, M., Merten, A., Grahmann, J., Boskovic, D., Tybussek, T., Rieblinger, K., and Wagner, J. (2016). Recent Advances and Applications of External Cavity-QCLs towards Hyperspectral Imaging for Standoff Detection and Real-Time Spectroscopic Sensing of Chemicals. *Photonics*, 3(28).

Rombach, S., Marx, M., Gu-Stoppel, S., and Manoli, Y. (2015). Low Power Closed-loop Driving Circuit for Piezoelectric Microscanners Based on Tuneable Capacitive Position Sensors. *Procedia Engineering*, 120, 63–66.

Roscher, K.U., Fakesch, U., Schenk, H., Lakner, H.K., and Schlebusch, D. (2003). Driver ASIC for synchronized excitation of resonant micromirrors. In *Proc. of SPIE, MOEMS Display and Imaging Systems*, volume 4985, 121–131.

Sandner, T., Klose, T., Wolter, A., Schenk, H., Lakner, H.K., and Davis, W. (2004). Damping analysis and measurement for a comb-drive scanning mirror. In *Proc. of SPIE, MOEMS and Micromachining*, volume 5455.

Sandner, T., Wildenhain, M., Gerwig, C., Schenk, H., Schwarzer, S., and Wölfelschneider, H. (2010). Large aperture MEMS scanner module for 3D distance measurement. In *Proc.of SPIE, MOEMS and Miniaturized Systems IX*, volume 7594, 75940D–11.

Schenk, H., Dürr, P., Haase, T., Kunze, D., Sobe, U., Lakner, H., and Kuck, H. (2000). Large deflection micromechanical scanning mirrors for linear scans and pattern generation. *IEEE Journal of Selected Topics in Quantum Electronics*, 6(5), 715–722.

Schroedter, R., Schwarzenberg, M., Dreyhaupt, A., Barth, R., Sandner, T., and Janschek, K. (2017). Microcontroller based closed-loop control of a 2D quasi-static/resonant microscanner with on-chip piezoresistive sensor feedback. In *Proc. of SPIE, MOEMS and Miniaturized Systems XVI*, volume 10116, 1011605.

Urey, H., Holmstrom, S., Baran, U., Aksit, K., Hedili, M.K., and Eides, O. (2013). MEMS scanners and emerging 3D and interactive Augmented Reality display applications. In *Proc. of Transducers Eurosensors XXVII: Conf. on Solid-State Sensors, Actuators and Microsystems*, 2485–2488.

Van Lierop, D. and Khah, K.S. (2019). Mirror device having leaf spring with openings. US Patent US20190129163A1.

Yazdi, N., Kulah, H., and Najafi, K. (2004). Precision readout circuits for capacitive microaccelerometers. In *Proc. of IEEE SENSORS*, volume 1, 28–31.

Yoo, H.W., Brunner, D., Thurner, T., and Schitter, G. (2019). MEMS Test Bench and Its Uncertainty Analysis for Evaluation of MEMS Mirrors. In *Proc. of 8th IFAC Symposium on Mechatronic Systems*, volume 52(15), 49–54.

Yoo, H.W., Druml, N., Brunner, D., Schwarzl, C., Thurner, T., Hennecke, M., and Schitter, G. (2018). MEMS-based lidar for autonomous driving. *e & i Elektrotechnik und Informationstechnik*, 135(6), 408–415.